Florian REGNIER[1,2], Antoine RILLAERTS[1,2], Vincent LEMAUR[1], Pascal VIVILLE[2*], Jérôme CORNIL[1*]
[1] Laboratory for Chemistry of Novel Materials, University of Mons, 7000 Mons, Belgium
[2] Materia Nova, Research and Development Center, 7000 Mons, Belgium
pascal.viville@materianova.be, jerome.cornil@umons.ac.be

A Joint Theoretical and Experimental Characterization of the Rising Star Y6 Acceptor in Organic Solar Cells – From Molecules to Devices

Abstract
For several years, climate changes and energy crisis have pushed the scientific community to develop sustainable and environmentally friendly technologies. This has notably given rise to the field of organic electronics aiming at exploiting organic materials as active layers in devices such as field-effect transistors (OFETs), photovoltaic devices (OPVs) or the well-marketed light-emitting diodes (OLEDs). The OPV technology is considered as a promising candidate to contribute to the energy transition although the devices still need to be improved in terms of performance and stability, especially via the development of new materials. In this context, we report here a joint theoretical and experimental characterization of the highly promising Y6 molecule used as acceptor in the last generation of devices. We demonstrate in particular that the solvent used for depositing the active layer (here chloroform versus chlorobenzene) strongly impacts their morphology, and in turn the solar cell performances.

1. Introduction

Over the past 40 years, climate changes and the resulting energy crisis have been steadily growing [1-3]. This phenomenon has been originating from the Industrial Revolution, a period characterized by an excessive increase in demand and consumption of energy as well as an extreme dependence on fossil fuels (gas, coal, oil, petroleum) [3-4]. Today, this demand is still increasing mainly due to the population growth and rapid development of technology [2-3]. However, the use of fossil fuels to fulfil this demand generates greenhouse gas emissions, such as the release of carbon dioxide (~35 billion tons in 2021) [5-6] which directly impacts environment and climate [2]. Moreover, fossil fuel resources are becoming limited and are likely to get exhausted soon, thus leading to possible socio-political conflicts, discontinuity or interruption of supply and sudden fluctuations of prices as we are currently facing [2]. On the basis of this emergency, a rethinking of our production methods as well as of our daily energy consumption is undoubtedly necessary to ensure the survival of the human race and all other living species of the planet in an ideally carbon-neutral future.

One well-accepted solution to promote the energy transition is the use of renewable resources. These technologies have the advantages to be sustainable, clean, abundant and to emit limited quantities of CO_2 during their life cycle; they can be easily developed in areas far away from cities and exhibit low operating and maintenance costs compared to more conventional fossil fuel technologies [2]. Among renewable energies, the

https://doi.org/10.52809/cn2022.vtzh2153

solar energy is the most significant exploitable energy source [3,7]. Indeed, the actual available capacity of solar energy on the surface of Earth is estimated at 600 TW [8], which is larger than our annual energy consumption of 13 TW [7-8] and much larger than those estimated for all other renewable technologies, such as hydroelectricity (0.5 TW), geothermal energy (12 TW) or wind energy (2 to 4 TW) [7-8]. Therefore, even if solar energy is intermittent, it represents an inexhaustible and universal energy source which exploited in different ways including solar thermal (e.g., solar tower or solar parabolic trough), bioenergy (photosynthesis), solar photovoltaic or photocatalytic applications [2-3].

1.1. The photovoltaic technology

Solar energy is typically collected with photovoltaic devices (PVs) that convert light into electricity. The physical phenomenon responsible for this conversion is called the "photovoltaic effect" discovered in 1839 by the French physicist Edmond Becquerel [3,9-10]. The original version of PVs, accounting for over 90% of the actual market [3,11], includes monocrystalline or polycrystalline silicon wafers [11-12]. Although their actual conversion yield, called "Power Conversion Efficiency" (PCE or η) reaches 27.6% at the laboratory scale [13], silicon solar cells (Si-SCs) have many drawbacks such as poor light absorption [14-15], high weight due to the large thickness of the layers required to absorb enough light [14-15] and high energy-consuming production steps due to purification processes required to ensure an efficient operation of the devices [14,16]. Such limitations have motivated the scientific community to elaborate other technologies, notably through the development of new alternative materials to substitute silicon in photovoltaic modules. To date, the intensive efforts have led to two additional generations of PV cells: (i) thin-film solar cells in which the dominant materials are amorphous silicon, cadmium telluride (CdTe) or copper indium gallium diselenide (CIGS) and (ii) an emerging category of devices including dye-sensitized solar cells (DSSCs), perovskite solar cells (PSCs) or organic solar cells (OSCs) [11-12].

Organic solar cells integrate semiconducting polymers or small organic molecules in the light absorbing layer [16-18]. They have been receiving an extensive interest due to their numerous advantages including: (i) light weight (~10 times lighter than Si-SCs) [17,19-20], allowing their use on any vertical support; (ii) good mechanical flexibility [17,19] allowing their deposition on any surface (for example, corrugated support or textile); and (iii) the possibility to fabricate semi-transparent devices [20-21]. OSCs can also be produced by simple, solvent-compatible and low-cost processes [17-19] thanks to the high solubility of organic materials in various solvents. Their processing typically carried out by printing techniques (e.g., spin-coating, slot-die, inkjet, roll-to-roll…) [18], can cover large surfaces with a small quantity of material (~1 g/m^2) [20], while maintaining high efficiencies and limiting the amount of CO_2 emitted during their manufacturing. OSCs are therefore emergent actors for the development of a highly efficient, environmentally friendly and large-scale technology in the field of organic electronics.

1.2. Device architecture and operating principle of OSCs

OSCs are typically made of an organic photoactive layer containing one electron accepting material (typically small molecules referred abusively as n-type in analogy with Si- SCs) and one electron donating material (typically polymers often described as p-type). They are deposited as two juxtaposed layers or as a bulk heterojunction. The active layer is sandwiched between two electrodes, typically aluminium and the transparent and metallic indium tin oxide (ITO) deposited on glass or plastic substrates [18,22-24], see **Figure 1**.

The general working principle of a bilayer solar cells, presented in **Figure 2**, can be divided into 5 main steps: (1) photon absorption and generation of an electron-hole pair, referred to as exciton; (2) exciton diffusion towards the donor-acceptor interface; (3) formation of an interfacial charge-transfer state and its dissociation into free charge carriers; (4) charge transport to the corresponding

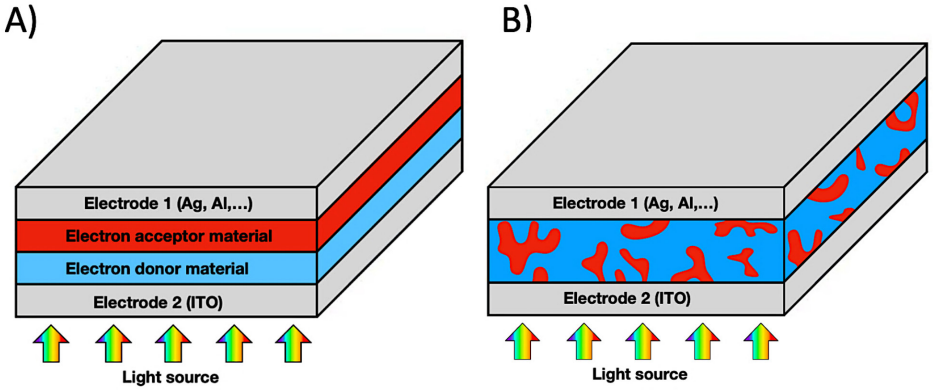

Figure 1: Architecture of (A) a bilayer solar cell and (B) a bulk heterojunction (BHJ) solar cell (B). The red and blue colors denote respectively the acceptor and donor material.

electrodes; and (5) charge collection at each electrode [25-27]. To efficiently convert light into electricity and achieve high performances, organic solar cells should meet several requirements in order to optimize each of these steps.

The use of a single organic material does not allow for the generation of a photocurrent. Indeed, the high stability of the excitons formed within organic materials makes their dissociation difficult under ambient conditions. The binding energy of excitons (E_b) results from the strong Coulomb attraction between the photogenerated hole and electron. Due to the low dielectric constant (ε_r) of organic materials, typically between 2 and 4, E_b is typically larger than 0.3 eV in semiconducting polymers and can reach up to 1 eV in small molecules due to charge spatial confinement in a small volume [28-29].

The binding energy is thus much higher than the thermal energy at room temperature (~25 meV), thus preventing the dissociation of excitons within the bulk of a single organic material [28-29]. This is why it is necessary to introduce a second organic material in the active layer with a proper positioning of the HOMO and LUMO levels of the two components to promote free charge carrier generation [28,30]. The donor molecule will be characterized by a smaller

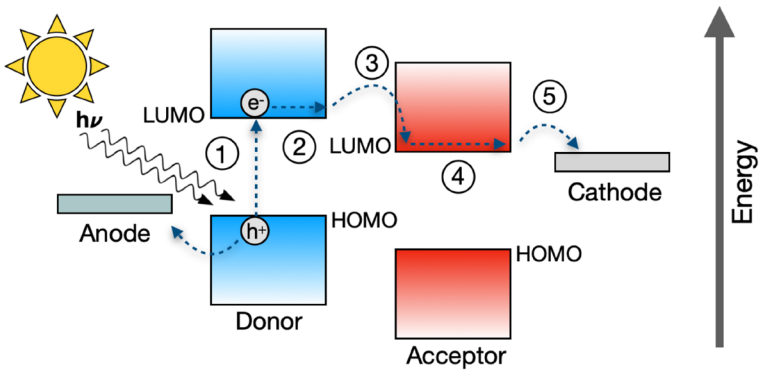

Figure 2: General working principle of a bilayer solar cell (h^+ stands for hole and e^- for electron).

ionization potential (lower HOMO level) and the acceptor by a stronger electron affinity (deeper LUMO) [25-28]. Therefore, if the exciton is generated on the donor compound, the energy difference between the LUMO of the acceptor and that of the donor (ΔE_{LUMO}) must be large enough to exceed the Coulombic attraction and ensure a photoinduced electron transfer, but not too large to avoid the loss of too much energy. Similarly, for an excitation on the acceptor, the photoinduced hole transfer is favorable if the energy difference between the HOMO of the donor and the HOMO of the acceptor (ΔE_{HOMO}) is strong enough to overcome the binding energy of the exciton, as figured out in **Figure 3**.

Although bilayer solar cells are the simplest to produce, their architecture endows only one planar D-A (donor-acceptor) interface for exciton dissociation, leading to cut short efficiencies [22,28,30]. Indeed, due to its short lifetime (< 1 ns), the diffusion length of an exciton is typically limited to a few tens of nanometers [22,25,28] and only excitons generated near the D/A interface can contribute to the charge generation [28]. This major drawback has led to the concept of bulk heterojunction (BHJ) [18,25,28] in which the active layer can be described as an interpenetrating network of donor and acceptor materials at the nanoscale [22,25]. Accordingly, most of the generated excitons can thus rapidly reach an interface before their recombination to be dissociated into free charge carriers that will then be transported through percolation pathways toward the respective contacts for collection [22,25]. On the negative side, this structure requires a precise control of the morphology to reach the most appropriate phase separation [22,25], which is still a huge current challenge.

In the BHJ device structure, thin inorganic or organic intermediate layers can be introduced between the active layer and electrodes to facilitate charge transport and charge collection, as shown in **Figure 4** [22,25,31-33]. These extra layers allow avoiding direct contact between the photoactive material and electrode, thus preventing exciton recombination at the contacts [32-33] and dictate the charge collection direction (i.e., polarity of the device) by blocking selectively holes at the cathode and electrons at the anode [22,24,32]. Two architectures are actually conceivable: the conventional or direct structure in which electrons are collected at the aluminium electrode and the

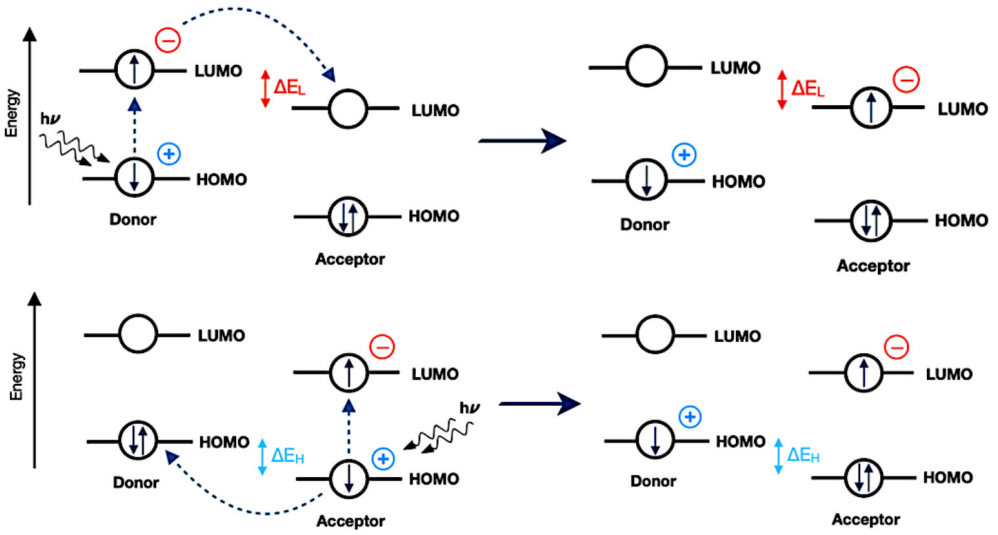

Figure 3: Schematic representation of photoinduced electron transfer (upper figure) and photoinduced hole transfer (lower figure) when the exciton is formed on the donor or on the acceptor respectively. In both cases, an interfacial charge transfer state is created with a hole on the HOMO of the donor and an electron on the LUMO of the acceptor.

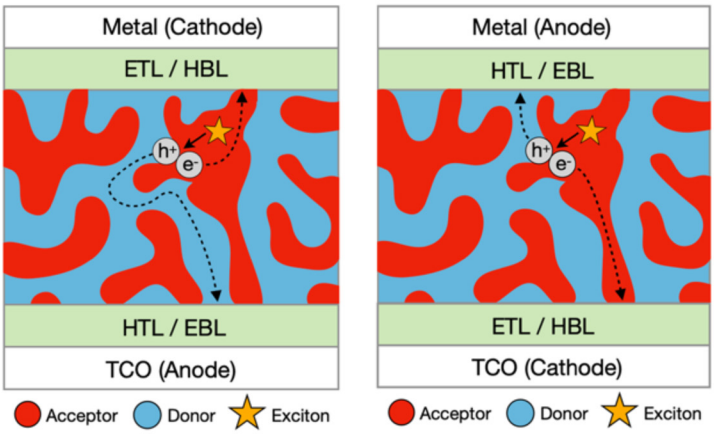

Figure 4: Architecture of conventional (left figure) and inverted (right figure) BHJ organic solar cells. HTL [HBL] denotes Hole Transport [Blocking] Layer and vice versa for electrons.

inverted structure in which electrons are collected at the ITO contact [23]. The blocking layers also prevent damaging chemical reactions or metallic ions diffusion at the electrode/organic interface [22,33-34], thus helping to increase the stability and hence lifetime of the devices. It is worth stressing that the choice of interlayers is limited to a few materials because these must offer simultaneously good charge transport properties, adapted electronic level matching at the photoactive layer/electrode interface, good chemical stability and high transparency to the visible solar irradiation [22,24]. The widely-used hole blocking layers (HBLs) / electron-transporting layers (ETLs) are LiF, TiO_x, ZnO and SnO_2 while electron-blocking layers (EBLs) / hole-transport layers (HTLs) are often WO_3, V_2O_5, MoO_3 and poly(3,4-ethylenedioxythiophene) polystyrene sulfonate (PEDOT:PSS) [3,23-25,31].

1.3. Device characterization

The photovoltaic performances are estimated from current density-voltage (J(V)) curves obtained both under illumination and in the dark, see **Figure 5** [3,30].

By convention, the illuminated curve must be recorded under 1 sun Air Mass 1.5 (AM~1.5 1000 W/m^2) conditions [8,30,35-36] in which the light source simulates the sun irradiation on Earth at an angle of about 48° from the zenith [30,36].

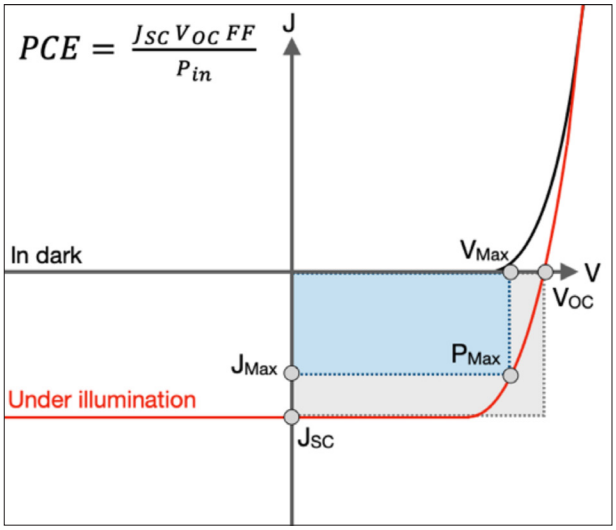

Figure 5: Typical current density-voltage (J(V)) curves obtained from OSCs characterization. The illuminated and dark curves are plotted in red and black, respectively.

From J(V) curves, it is possible to extract the power conversion efficiency, denoted PCE [16,30] expressing the amount of electrical power (P_{out}) produced by the solar cell relative to the power of the incident light radiation (P_{in}) [16,30]. P_{out} is given by the product of three parameters namely the short-circuit current (J_{SC}), open-circuit potential (V_{OC}) and fill factor (FF) [16,30]. Obtaining high efficiency OSCs requires maximizing these three key parameters (J_{SC}, V_{OC}, FF).

The short-circuit current (J_{SC}) corresponds to the current density that flows through the illuminated solar cell when no electrical potential is applied

[22,28,30]. J_{SC} depends on the efficiency of light absorption, the mobility of charge carriers and is reduced by charge recombination phenomena [16]. The open-circuit potential (V_{OC}) represents the value of the bias at which there is no current in the device [28,30]. The maximum value of V_{OC} matches the energy difference between the LUMO of the acceptor and the HOMO of the donor [18,33,37], but is further reduced with the charge recombination phenomena occurring in the active layer. The fill factor (FF) is defined as the ratio of the maximum power actually delivered by the device (area of the blue rectangle, $P_{max} = J_{max} \times V_{max}$) and the ideal maximum power output (area of grey rectangle) obtained when $P_{max} = J_{SC} \times V_{OC}$, see **Figure 5** [30,38]. This FF parameter is affected by two types of resistance across the device: the series resistance (R_S) and the parallel resistance (R_{Sh}) [22,37]. R_S depends on the interface contact resistance between the stacking layers and the bulk resistance of each material [39]. This resistance can be estimated from the slope of the J(V) curve near V_{OC} and must be as low as possible ($R_S \rightarrow 0$) [37,39]. The R_{Sh} parameter is impacted by any current leakage from the edge of the cell and from pinholes in the film or by the presence of energy traps typically associated to energetic disorder among the transport levels. This resistance should be as high as possible ($R_{Sh} \rightarrow \infty$) to increase FF and is estimated from the slope of the J(V) curve near the J_{SC} [37,39].

1.4. The birth of NFA molecules

The first generation of OSCs was based on active layers including donor polymers, such as the well-known poly(3-hexylthiophene) (P3HT), combined to the prototypical fullerene-type acceptor molecule (FAs) 1-(3-methoxycarbonyl) propyl-1-phenyl[6,6]C_{61} ($PC_{61}BM$) [17,40-41]. Although PCBM presents interesting isotropic charge transport properties and a high electron affinity [17], devices involving them exhibited limited conversion efficiency, between 5% and 11% [40-41], mainly due to the poor absorption properties of fullerenes, chemical stability problems and morphological instability linked to the spherical shape of the fullerene compounds [19,26,40,42]. Tremendous molecular design efforts have thus been carried out to develop new classes of non-fullerene acceptor molecules (NFAs). Among them, the most extensively studied compounds feature an A-D-A structure as represented by the ITIC-series that appeared in 2015, as well as an A-D-A'-D-A-type structure such as in the Y-series developed in 2019 (**Figure 6**) [17,19].

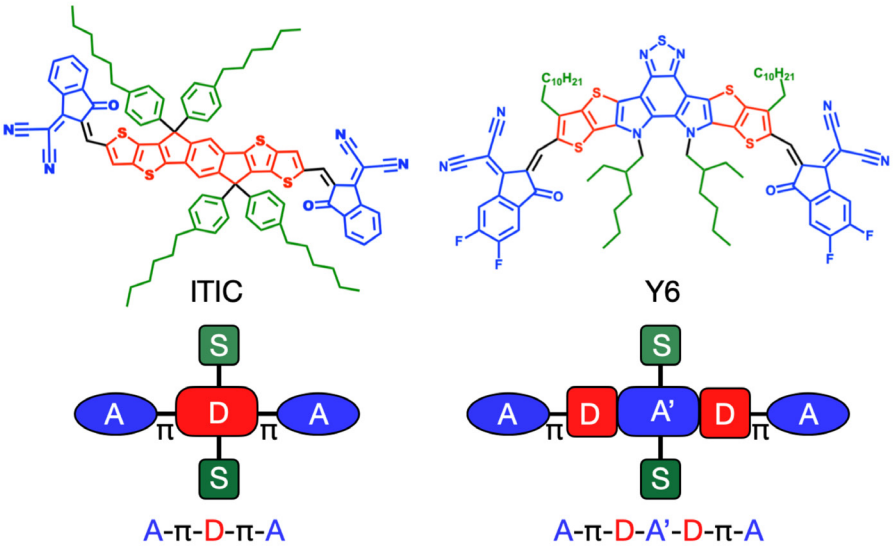

Figure 6: Molecular structure of ITIC and Y6 NFA. The distinctive domains are highlighted: acceptor unit (blue), donor unit (red) and side chains (green).

Today, NFAs have pushed the power conversion efficiency (PCE) beyond 15% at the laboratory scale after full device optimization and adequate choice of additives [19,43-44]. This boost in photovoltaic performances can be undoubtedly attributed to the key assets of NFAs compared to FA derivatives, such as a significant absorption of the solar emission or a very modular structure, which allows for fine tuning the solid-state packing and electronic/optical properties driving the efficiency of the different steps in solar conversion [19,26,40,42,45]. Developing new materials with enhanced performance definitively requires now the establishment of structure-properties-device performance that are often overlooked when searching for formulations yielding the highest power conversion efficiency.

In this paper, we contribute to this endeavor by reporting a fundamental study of the electronic, optical and morphological properties of the molecular electron acceptor Y6 currently considered as a rising star in the field. By combining theoretical modelling, experimental characterizations and device fabrication, we highlight some factors explaining why this NFA material leads to higher conversion efficiencies compared to the pristine FA compounds and propose different guidelines for the development of new compounds.

2. Results and discussion

2.1. Theoretical modelling

The first part of our study starts with a theoretical investigation of the structural, electronic and optical properties of the Y6 molecule. We performed here quantum-chemical calculations at the DFT (Density Functional Theory) level using the LC-ωHPBE functional and a 6-31G(d,p) basis set [46-48], as implemented in Gaussian 16 (revision A.03) [49]. All alkyl side chains in the molecular structure were replaced by methyl groups (-CH_3) to reduce calculation time [50-51]. Changing the length of the side chains does not affect the properties of isolated molecules and should not strongly impact the structural properties of the conjugated central core inferred in presence of the methyl groups. The optimized molecular geometry obtained with an adjusted ω value of 0,1068 $Bohr^{-1}$ is presented in **Figure 7**. The molecule adopts a U-shaped geometry with a permanent dipole moment of 1.7 Debye along the Z-axis. This structural change, compared to the previous S-shaped ITIC-series

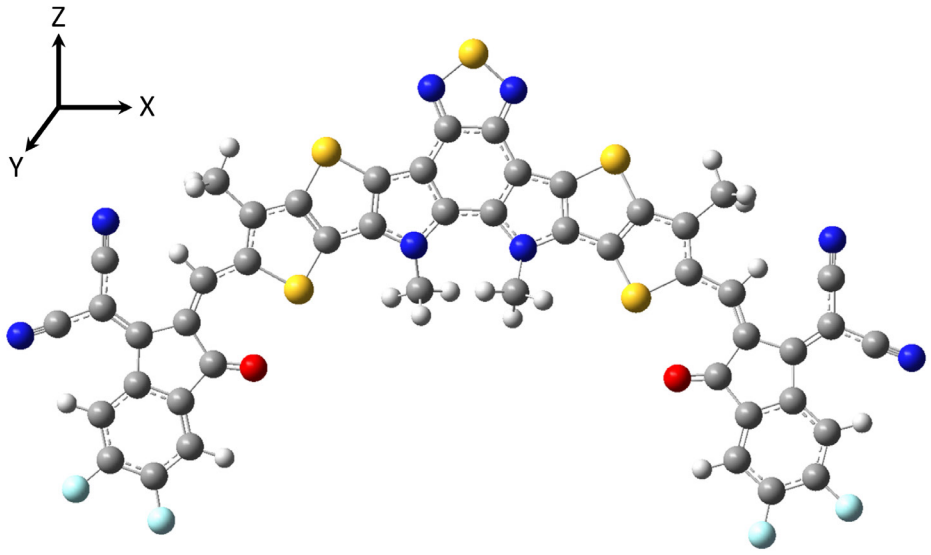

Figure 7: Optimized structure of Y6 obtained from LC-ωHPBE/6-31G(d,p) DFT calculations.

with no dipole, is likely to impact intermolecular interactions between molecules in the condensed phase (i.e., the molecular packing) and hence the charge transport properties [26,52]. In spite of a slight central twist of 12.7° induced by steric hindrance between the inner alkyl groups, Y6 exhibits a pronounced molecular flatness which is favorable to extent π-electron delocalization over the molecular backbone.

The shape of the frontier orbitals (FOs) has also been computed, while considering solvent effects via a Polarizable Continuum Model (PCM); we consider here chloroform (ε = 4.71) and chlorobenzene (ε = 5.69) commonly used in the literature due to their excellent dissolution ability of NFAs [53-55]. Since the results obtained are similar in both solvents, the following discussion is only focused on the results obtained in chloroform. As shown in **Figure 8**, the LUMO of Y6 is completely delocalized all along backbone while its HOMO is mostly localized on the center [51,56].

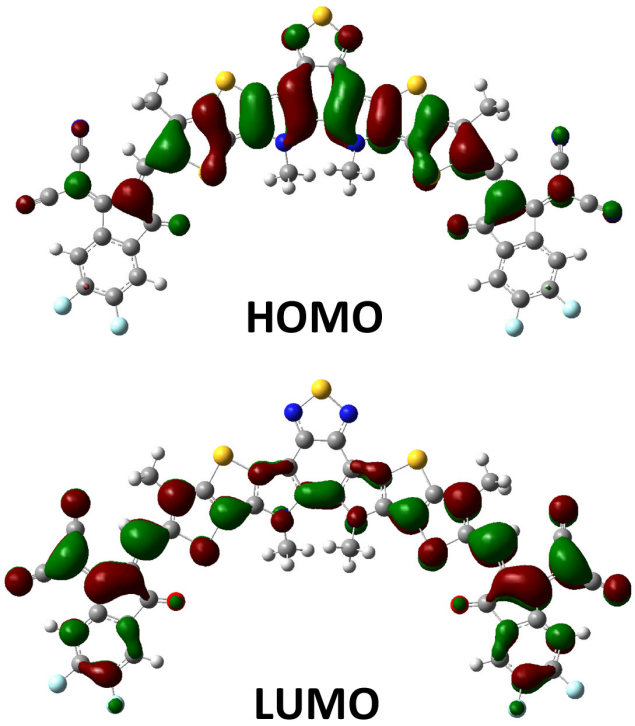

Figure 8: HOMO/LUMO wavefunction distribution in Y6 obtained from LC-ωHPBE/6-31G(d,p) DFT calculations taking into account solvent effect of chloroform. The wavefunction sign is represented by red (positive) and green (negative) colors.

This high delocalization of the LUMO level is an interesting feature to promote intermolecular electron transport between adjacent molecules in the condensed phase.

A Mulliken population analysis, presented in **Figure 9**, has been conducted to study the donor/acceptor character of the molecular domains.

The terminal groups, thienothiophene core units and the BT group fused to the neighboring pyrroles, as highlighted in **Figure 10**, have a respective charge of -0,4 |e|, +0,6 |e| and -0,2 |e|. Moreover, the Mulliken analysis points to attractive interactions between the positive charge on the sulfur atom of one thiophene of the core (+0.38 |e|) and the negative charge on the adjacent oxygen atom located on the terminal group (-0.47 |e|). This S-O coulombic attractive interaction (d_{S-O}~2.7 Å) might trigger a conformational blocking favoring further the coplanarity of the molecule [44,57].

In order to investigate the impact of end-group halogenation on the optoelectronic properties in existing Y derivatives, similar theoretical calculations were carried out on the optimized structures of the non-halogenated and chlorinated derivatives of Y6, respectively Y5 (BTP) and Y7 (BTP-4Cl). The optimized value of ω is also 0,1068 $Bohr^{-1}$ for both molecules. Halogenation of terminal groups does not significantly impact the electronic gap ($E_{Gap} = E_{HOMO} - E_{LUMO}$) as illustrated in **Figure 11**, or frontier orbital localization whatever the solvent employed but lowers progressively the energy of the frontier electronic levels when going from Y5 to Y7. Therefore, the terminal group halogenation appears to be an effective strategy to modify the V_{OC} parameter in OSC devices without impacting the absorption spectra of the molecules.

We have finally simulated the absorption spectrum of Y6 and its derivatives in chloroform and chlorobenzene, see **Figure 12**. All graphs are plotted with a full width at half-maximum (FWHM) of 0.25 eV. In spite of the small permanent dipole moment, an interesting observation is the lack of solvatochromism effect (shift of the lowest absorption band by only 6 nm~0.02 eV between

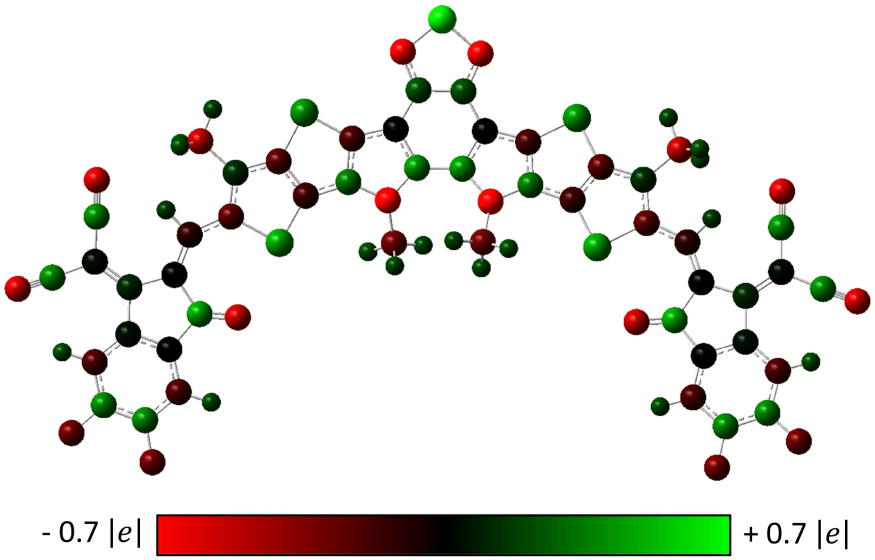

Figure 9: Mulliken population analysis for the Y6 molecule, as obtained at the LC- ωHPBE/6-31G(d,p) DFT level.

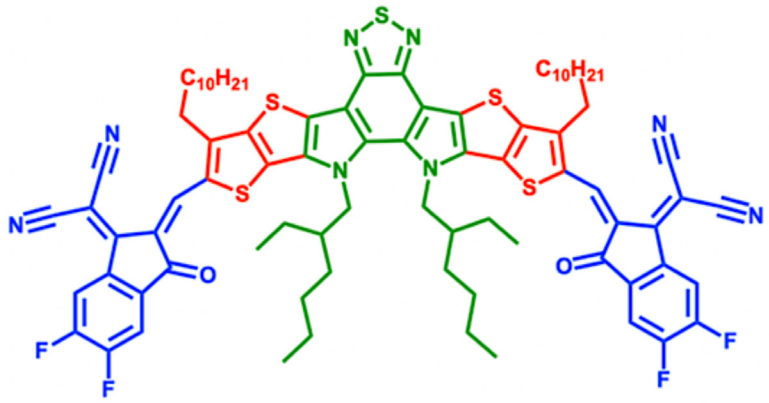

Figure 10: Terminal groups (blue), thienothienophene core units (red) and BT group fused to the neighboring pyrroles (green) on Y6 molecule.

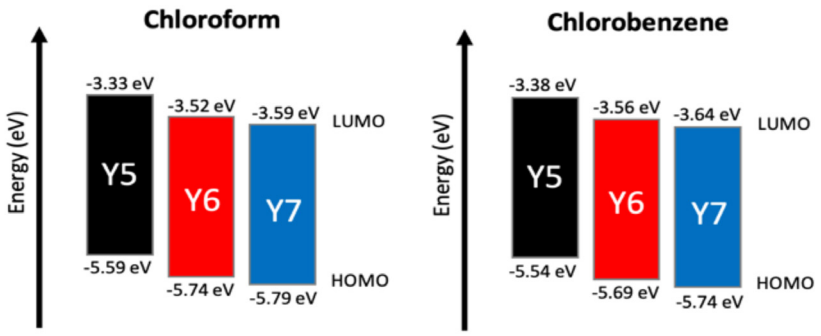

Figure 11: HOMO and LUMO energies obtained from LC-ωHPBE/6-31G(d,p) DFT calculations for Y5, Y6 and Y7 in chloroform (left figure) and chlorobenzene (right figure).

the two solvents) which points to a weak impact of solvent on the optical transitions of the molecules. As expected from the previous considerations, the halogenation of the terminal group has a minimal impact on the optical band gap whatever the solvent used. Indeed, the lowest optical absorption band, corresponding to a transition between the ground state (S_0) to the first excited state (S_1), is located at 615 nm (2.01 eV), 625 nm (1.98 eV) and 635 nm (1.95 eV) for Y5, Y6 and Y7 in chloroform while they lie at 621 nm (2.00 eV), 631 nm (1.97 eV) and 641 nm (1.93 eV) in chlorobenzene, respectively. The calculated molar absorption coefficient (ε_λ) is about 1 10^5 M^{-1} cm^{-1} for each derivative, denoting the very good absorption properties of these compounds compared to fullerene derivatives ($\varepsilon_\lambda < 0.5\ 10^5\ M^{-1}\ cm^{-1}$) [58]. An overlap factor (ϕ_s) between the hole density (ρ_h) and electron density (ρ_e) associated to first excited state (S_1), mostly described by a HOMO → LUMO transition, has been determined to be 0.62 [56,59]. This points to a good compromise between the charge-transfer state character of S_1 ($\phi_s \rightarrow 0$) which facilitates exciton dissociation and a local character ($\phi_s \rightarrow 1$) required for efficient optical absorption [59].

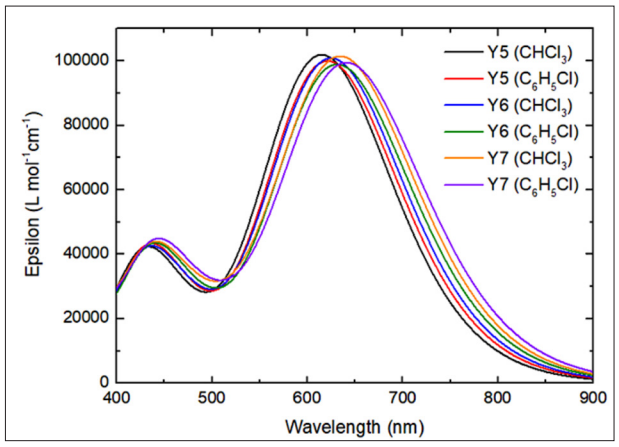

Figure 12: Simulated absorption spectra obtained from TD-DFT/LC-ωHPBE/6-31G(d,p) calculations for Y5, Y6 and Y7 in chloroform and chlorobenzene.

2.2. Optical properties

The experimental UV-visible normalized absorption spectra of Y6 as well as the electron donor polymer PM7 in both host solvents are presented in **Figure 13**.

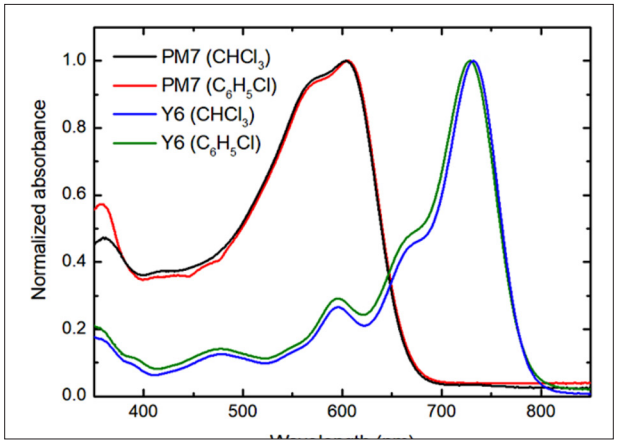

Figure 13: Normalized absorption spectra of Y6 and PM7 in CF and CB solution (C = 6.25 10^{-3} mg/mL).

The absorption maxima are located at 604 nm (2.05 eV) and 732 nm (1.69 eV) for PM7 and Y6 respectively in chloroform [60-61] while they lie at 605 nm (2.05 eV) and 729 nm (1.70 eV) in chlorobenzene, thus reflecting the absence of solvatochromism, as predicted by our theoretical study. From Beer-Lambert's law ($A_\lambda = \varepsilon_\lambda.L.C$) [62-63] with the absorbance value at a given wavelength, L the optical path length (cm) and C the molar concentration of absorbing species in solution (mol L^{-1} or M), the molar absorption coefficients (ε_{max}) at λ_{max} are determined to be 1.75 10^5 $M^{-1}cm^{-1}$ for Y6, in deep consistency with the theoretical estimates yielding values around 10^5 $M^{-1}cm^{-1}$.

UV-Vis spectroscopy analyses on PM7 and Y6 thin films on glass substrate, see **Figure 14**, show a red-shifted absorption compared to the spectra obtained in solution.

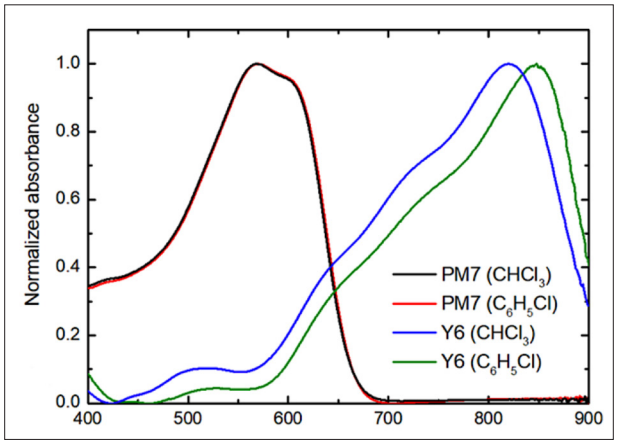

Figure 14: Absorption spectra of PM7 and Y6 films prepared from chloroform and chlorobenzene.

For the PM7 polymer, the $S_0 \rightarrow S_1$ absorption peak is shifted by 3 nm (0.01 eV) in both solvents, while this shift is more pronounced in the case of Y6 with the absorption peak in film located at 819 nm in chloroform (shift ~ 0.18 eV) and 848 nm in chlorobenzene (shift ~ 0.24 eV). The unusually large bathochromic shift observed in the case of Y6 is likely to originate from pronounced π-π and/or electrostatic interactions [51,61]. From the formula $\alpha = (\frac{1}{d})\ \ln\ (\frac{1}{T})$, where d represents the film thickness (cm) and T the transmittance [64], the average absorption coefficient (α) in the neat films of Y6 is estimated to be 2.81 10^5 cm^{-1}. Such a high absorption coefficient and the high complementarity with the PM7 polymer absorbing in the 600 nm-900 nm range are highly beneficial to maximize the collection of photons in the visible range of wavelengths of the solar spectrum, and hence to increase the value of the J_{SC} parameter [26,51].

2.3. Morphological properties

The surface morphology of non-annealed PM7 and Y6 thin films prepared from the two host solvents as well as of non-annealed PM7:Y6 blend in the [1:1] weight ratio typically used in the active layer was investigated by Atomic Force Microscopy (AFM). The surface of the PM7 film, shown in **Figure 15**, exhibits a similar smoothness in both solvents, with the presence of 30-70 nm-long fiber-like aggregates [65-66].

The root-mean-square surface roughness (R_q) is 1.0 nm and 0.6 nm in chlorobenzene (CB) and chloroform (CF), respectively. Concerning the Y6 neat films, see **Figure 16**, large grains with a size between 40 nm and 110 nm are visualized with both solvents. More aggregation effect is observed in the case of the CB-processed film, translating to a higher R_q value of 5.1 nm compared to CF-processed film with R_q = 2.8 nm; this is mostly likely due to a lower solubility of Y6 in CB.

AFM image of a 100-nm PM7:Y6 [1:1] blend, see **Figure 17**, shows different morphologies as a function of the solvent used for their processing. The films prepared from CB exhibit a granular morphology similar to Y6 films. A high R_q of 4.7 nm points to strong aggregation of the Y6 molecules in the mixture. This large domain separation is detrimental for exciton dissociation in the device [43,65]. In contrast, a 100-nm thin film of PM7:Y6 [1:1] prepared from CF shows a morphology quite similar to that of PM7 films alone without grain formation. The R_q is significantly reduced down to 0.9 nm, thus attesting of the good miscibility of the two components.

2.4. Device fabrication and characterization

To evaluate the photovoltaic performances of the 100 nm-thick PM7:Y6 [1:1] active layer deposited from chlorobenzene or chloroform, a series of non-optimized OSCs with an inverted device

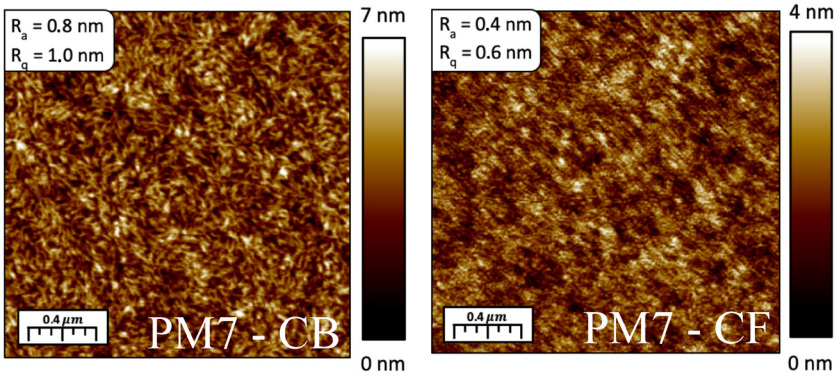

Figure 15: AFM images (2x2 µm²) for PM7 pure films prepared from chlorobenzene (left) and chloroform (right). Their thickness are 150 nm and 170 nm, respectively.

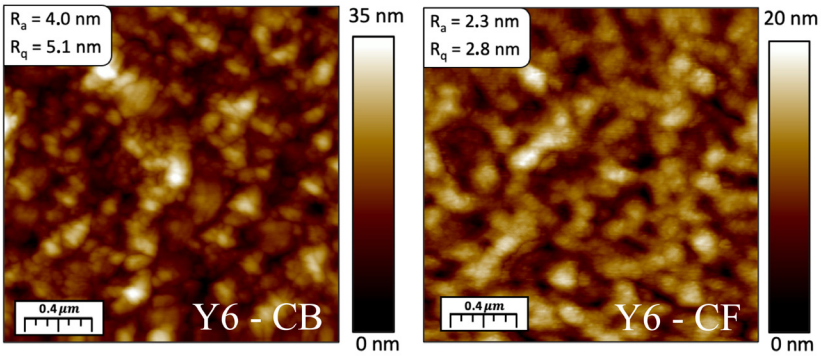

Figure 16: AFM images (2x2) for neat films of Y6 prepared from chlorobenzene (left) and chloroform (right) solutions. Their thickness is 60 nm for Y6 in chlorobenzene and 90 nm in chloroform.

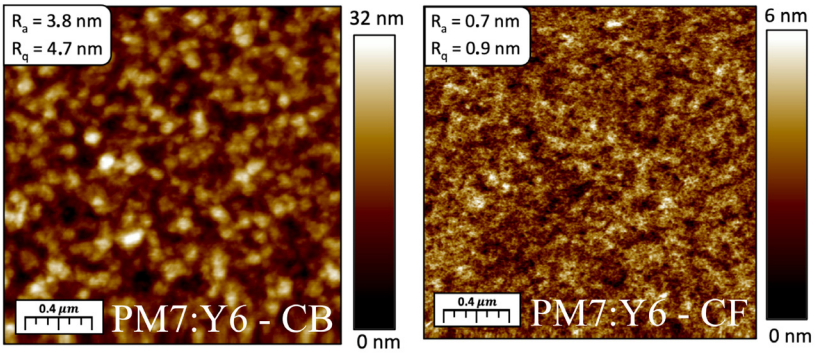

Figure 17: AFM images (2x2 µm^2) for blend films of PM7:Y6 prepared from chlorobenzene (left) and chloroform (right) solutions. Their thickness is 105 nm in chlorobenzene and 98 nm in chloroform.

architecture of the type Glass/ITO/Al/SnO_2/Active layer/MoO_3/Al were fabricated and characterized. In this device architecture, deposition of a thin Al layer on the ITO electrode allows for a reduction of the series resistances (R_s) of the devices. The SnO_2 HBL is deposited from a solution containing 0.5 mL of stock solution (2.5 wt% crystalline SnO_2 diluted in butanol) added in 2.6 mL of butanol. This solution was deposited by spin coating at a rotation speed of 3000 rpm for 30 seconds and annealed on a hot plate for 30 min at 150°C. The active layer was spin-coated in both solvents under inert conditions (Nitrogen Glovebox) at a speed of 1500 rpm during 60 seconds and annealed at 100°C for 10 min. The MoO_3 EBL was deposited by thermal evaporation as well as the Al counter electrode. All manufacturing steps (A), the energy diagram of the device (B) [25,44,67-68] and the thickness of each layer (C) are shown in **Figure 18**.

Table 1 summarizes the main characteristics of the fabricated solar cells with an active illuminated zone of 2.56 mm^2, as systematically averaged over 5 devices (D_x with x = 1, 2, …, 8) built from the same active layer (see red squares in **Figure 18-A**). Devices made of PM7:Y6 [1:1] deposited from chloroform show the highest performances with an averaged J_{sc} of 14.04 mA/cm^2, V_{OC} of 0.87 V and FF of 56.46 % leading to a PCE of 6.91 %. When using the chlorobenzene, we obtain a much lower current density of 10.43 mA/cm^2 but a higher FF of 61.44 %, leading together to a lower PCE of 5.25 %. The significant drop in J_{SC} can be mainly attributed to the granular morphology associated to a lower solubility of Y6 in chlorobenzene. The domain sizes (~ 50 to 150 nm) are indeed larger than the average exciton diffusion length (around 10-20 nm) [22], and hence not favorable for the exciton dissociation process and free carrier

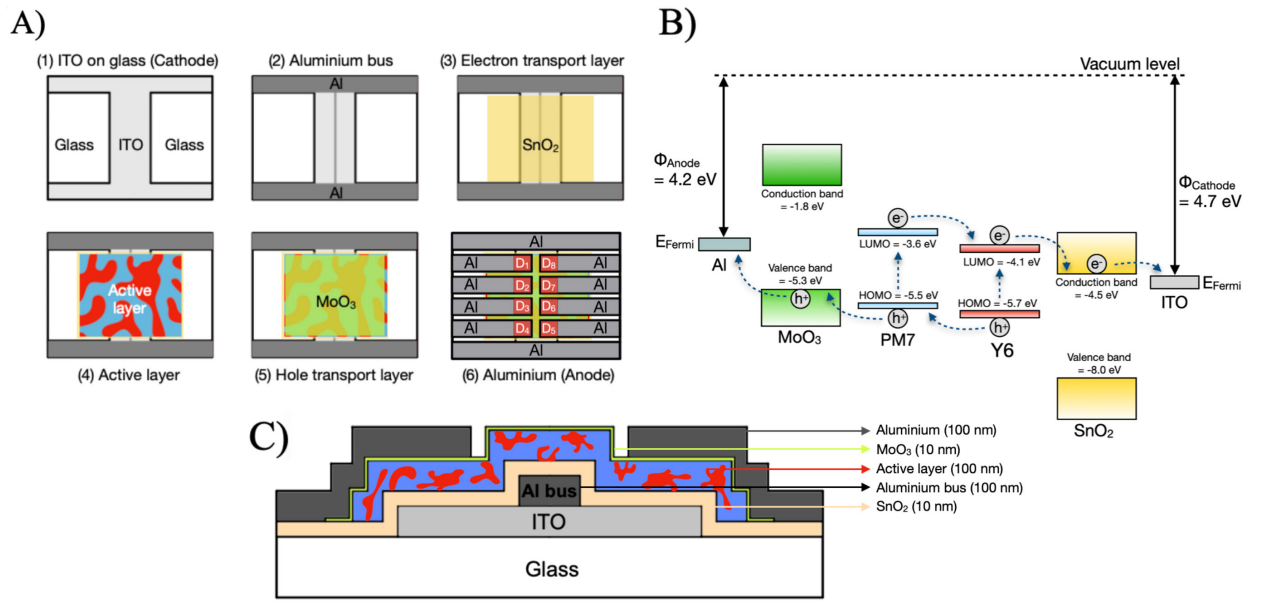

Figure 18: Manufacturing steps for the fabrication of the ITO/Al/SnO_2/PM7:Y6/MoO_3/Al of the eight devices $D_1 \rightarrow D_8$ in parallel (A), energy diagram of the electronic structure of the different layers illustrating the device operation from the charge generation to the charge collection (B) and side view (C) of the inverted OSCs device.

generation. The V_{OC} value is conserved around 0.8 V, indicating that the morphology changes do not drastically affect the efficiency of the charge recombination processes.

All blends yield small values of series resistances (R_{Series}) both in the dark and under illumination, thus pointing to good charge extraction and electrical contacts in the device. The slightly lower values in the case of chlorobenzene reflect a lower interface resistance between layers in the devices or a lower bulk resistance in the active blends [39]. Concerning the shunt resistances (R_{Sh}), all blends present a quite high value which points to the absence of significant leakage currents in the dark [39]. Under illumination, these values sharply decrease around 400-500 Ohm cm^2: this likely originates from the presence of energetic disorder (and hence charge carrier traps) that defines specific percolation pathways and prevent a homogeneous extraction of the charges from the active layer [39].

3. Conclusion

To sum up, we performed a combined theoretical and experimental study of the structural, optoelectronic and morphological properties of the widely used NFA Y6. The theoretical exploration points to a high LUMO delocalization,

Active layer [1:1]	Host solvent	J_{SC} (mA/cm²)	V_{OC} (V)	FF (%)	$R_{Serie\ Light}$ (Ohm cm²)	$R_{Serie\ Dark}$ (Ohm cm²)	$R_{Shunt\ Light}$ (Ohm cm²)	$R_{Shunt\ Dark}$ (Ohm cm²)	Morphology	PCE (%)
PM7:Y6	$CHCl_3$	14.04 +- 0.50	0.87 +- 0.01	56.46 +- 0.76	1.54 +- 0.17	1.60 +- 0.19	405.4 +- 10.36	46342.80 +- 20219.76	Filaments	6.91 +- 0.27
PM7:Y6	C_6H_5Cl	10.43 +- 0.41	0.82 +- 0.01	61.44 +- 0.92	0.70 +- 0.07	0.70 +- 0.07	532.20 +- 29.85	14708.80 +- 9820.29	Grains	5.25 +- 0.19

Table 1: Solar cell parameter values averaged over 5 devices on a single substrate.

in spite of the A-D-A'-D-A structure, which should favor intermolecular charge transport properties. The theoretical results also indicate that the halogenation of the terminal groups constitutes a very good strategy to modulate the open-circuit potential in OSCs without strongly impacting the absorption signature of NFAs. The comparison of simulated spectra in two solvents widely used experimentally (CF and CB) evidences a negligible solvatochromism effect on optical transitions, which has been further confirmed by experimental spectra. Spectroscopy analyses of Y6 films show an unexpectedly large bathochromic shift compared to solution, most probably as a result of pronounced π-π and/or electrostatic interactions in the solid state, whatever the host solvent used. Moreover, the high absorption coefficients of Y6 and its complementary with PM7 are highly beneficial to improve the J_{SC} parameter and by extension the PCE of OSCs. Concerning the morphology investigations of Y6 films, large grains are visualized from both solvents, but the higher roughness measured for CB films suggests that Y6 is less soluble in this solvent. A similar grain morphology is observed for the PM7:Y6 blend deposited from CB whereas a filament-like morphology is displayed in CF. A granular morphology in the PM7:Y6 blend is detrimental for the exciton dissociation processes, leading to lower values of J_{SC} and by extension to a lower PCE, as confirmed by the device characteristics. Altogether, this work has highlighted the high potential of the Y6 NFA for organic solar cells and in particular the importance of carefully choosing the solvent used for processing to optimize the morphology of the active layers, which plays a crucial role in defining the OSC performances.

Acknowledgments

The theoretical work was supported by the Consortium des 'Equipements de Calcul Intensif' funded by the Fonds National de la Recherche Scientifique (FR-FNRS) under Grant No.2.5020.11. A.R. thanks the 'Fonds pour la Recherche Industrielle et Agricole' (FRIA) for his Ph.D. grant. J.C. is an FNRS research director.

References

[1] Kandel, R. Le réchauffement climatique. Chapter 1: Introduction. *Paris cedex 14 : Presses Universitaires de France*. **2009**. 5-14. URL: https ://www.cairn.info/le-rechauffement-climatique--9782130570561-page-5.htm?contenu=resume

[2] Kamran, M.; R. Fazal, M. Renewable Energy Conversion Systems. Chapter 1: Fundamentals of renewable energy systems. *Elsevier Inc.* **2021**. 1-19.

[3] Bhaumik, S.; K. Saha, S.; K. Rath, A. New Research Directions in Solar Energy Technologies. Chapter 4: A Perspective on Perovskite Solar Cells. *Energy, Environment, and Sustainability.* Springer, Singapore. **2021**. 55-151. DOI: https://doi.org/10.1007/978-981-16-0594-9_4

[4] Ritchie, H.; Roser, M. Energy mix, Global primary energy: how has the mix changed over centuries? *Our World in Data*. **2022**.

[5] Liu, Z.; Deng, Z.; J. Davis, S. *et al*. Monitoring global carbon emissions in 2021. *Nature reviews earth & environment*. **2022**, *3*, 217-219. DOI: https://doi.org/10.1038/s43017-022-00285-w

[6] Ritchie, H.; Roser, M. CO_2 emissions, Global CO_2 emissions from fossil fuels. *Our World in Data*. **2022**.

[7] S. Lewis, N.; Crabtree, G., J. Nozik, A. *et al*. Basic Research needs for solar energy utilization, Report on the Basic Energy Sciences Workshop on Solar Energy Utilization. *Argonne National Laboratory*. **2005**. 7-10.

[8] Wang, G. Technology, manufacturing and grid connection of photovoltaic solar cells. Chapter 1: Basic Physics of Solar Cells. *John Wiley & Sons, Singapore*. **2018**.

[9] Labouret, A.; Cumunel, P.; Braun, J-P. *et al*. Cellules solaires, Les bases de l'énergie photovoltaïque. Chapter 3 : Cellules et panneaux photovoltaïques. *Dunod, Paris*. **2010**. 31-48.

[10] Riverola, A.; Vossier, A.; Chemisana, D. Nanomaterials for solar cell applications. Chapter 1: Fundamentals of solar cells. *Elsevier Inc.* **2019**. 3-33.

[11] Amin, N. Comprehensive guide on organic and inorganic solar cells, Fundamental Concepts to Fabrication Methods. Chapter 1: Principle of photovoltaics. *Elsevier Inc.* **2022**. 1-23.

[12] Bhujel, R.; P. Swain, B. Fabrication and characterization of silicon nanowires hybrid Solar cells: a review. *IOP Conference Series: Materials Science and Engineering.* **2018**, *377*, 012193. DOI: 10.1088/1757-899X/377/1/012193

[13] Abzieher, T.; Mowafak, A-J.; Kirstin, A. *et al*. Best Research-Cell Efficiency Chart. *NREL*. **2022**.

[14] M. Bagher, A. Comparison of organic solar cells and inorganic solar cells. *International Journal of Renewable and Sustainable Energy.* **2014**, *3*, 53-58. DOI: 10.11648/j.ijrse.20140303.12

[15] Irvine, S. Springer Handbook of Electronic and Photonic Materials. Chapter 46: Solar Cells and Photovoltaics. *Springer Science+Business Media*. **2006**. 1095-1106.

[16] Destruel, P. ; Seguy, I. Les cellules photovoltaïques organiques. *Techniques de l'Ingénieur*. **2004**. *25*. 1-11.

[17] Lu, B.; Wang, J.; Zhang, Z. *et al.* Recent progress of Y-series electron acceptors for organic solar cells. *Nano Select*. **2021**, *2*, 2029-2039. DOI: https ://doi.org/10.1002/nano.202100036

[18] Hösel, M.; Angmo, D.; C. Krebs, F. Handbook of organic materials for optical and (opto)electronic devices, Properties and applications. Chapter 17: Organic solar cells (OSCs). *Woodhead Publishing Limited*. **2013**. 473-507.

[19] Wei, Q.; Liu, W.; Leclerc, M. *et al*. A-D-A'-D-A non-fullerene acceptors for high-performance organic solar cells. *Science China Chemistry*. **2020**, *63*, 1352-1366. DOI: https://doi.org/10.1007/s11426-020-9799-4

[20] Riede, M.; Spoltore, D.; Leo, K. Organic Solar Cells – The Path to Commercial Success. *Advanced Energy Materials*. **2020**, *11*, 2002653. DOI: https://doi.org/10.1002/aenm.202002653

[21] Hai, J.; Luo, S.; Yu, H. *et al*. Achieving ultra-narrow bandgap non-halogenated non-fullerene acceptor via vinylene -bridges for efficient organic solar cells. *Materials Advances*. **2021**, *2*, 2132-2140. DOI: https://doi.org/10.1039/D0MA01017K

[22] Uddin, A. Comprehensive guide on organic and inorganic solar cells, Fundamental Concepts to Fabrication Methods. Chapter 2: Organic solar cells. *Elsevier Inc.* **2022**. 25-55.

[23] Wang, K.; Liu, C.; Meng, T. *et al*. Inverted organic photovoltaic cells. *Chemical Society Reviews*. **2016**, *45*, 2937-2975. DOI: https://doi.org/10.1039/C5CS00831J

[24] Lattante, S. Electron and Hole Transport Layers: Their Use in Inverted Bulk Heterojunction Polymer Solar Cells. *Electronics*. **2014**, *3*, 132-164. DOI: 10.3390/electronics3010132

[25] D.S. Fung, D.; C.H. Choy, W. Organic Solar Cells, Materials and Device Physics. Chapter 1: Introduction to Organic Solar Cells. *Green Energy and Technology*. Springer-Verlag, London. **2013**. 1-16. DOI: 10.1007/978-1-4471-4823-4_1

[26] Zhao, J.; Yao, C.; Umair Ali, M. *et al*. Recent Advances in High-performance Organic Solar Cells Enabled by Acceptor-Donor-Acceptor-Donor-Acceptor (A-DA'D-A) Type Acceptors. *Materials Chemistry Frontiers*. **2020**, *4*, 3487-3504. DOI: https://doi.org/10.1039/D0QM00305K

[27] Tu, Z.; Han, G.; Yi, Y. Barrier-Free Charge Separation Enabled by Electronic Polarization in High-Efficiency Non-fullerene Organic Solar Cells. *The Journal of Physical Chemistry Letters*. **2020**, *11*, 2585-2591. DOI: https://doi.org/10.1021/acs.jpclett.0c00405

[28] Scharber, M.C.; Sariciftci, N.S. Efficiency of bulk-heterojunction organic solar cells. *Progress in Polymer Science*. **2013**, *38*, 1929-1940. DOI: https://doi.org/10.1016/j.progpolymsci.2013.05.001

[29] Han, G.; Yi, Y. Origin of Photocurrent and Voltage Losses in Organic Solar Cells. *Advanced theory and simulations*. **2019**, *2*, 1900067. DOI: https://doi.org/10.1002/adts.201900067

[30] L. Benanti, T.; Venkataraman, D. Organic solar cells: An overview focusing on active layer morphology. *Photosynthesis Research*. **2006**, *87*, 73-81. DOI: https://doi.org/10.1007/s11120-005-6397-9

[31] Xu, B.; Zheng, Z.; Zhao, K. *et al.* A Bifunctional Interlayer Material for Modifying Both the Anode and Cathode in Highly Efficient Polymer Solar Cells. *Advanced Materials*. **2016**, *28*, 434-439. DOI: https://doi.org/10.1002/adma.201502989

[32] H. Park, J.; Lee, T-W.; Chin, B-D. *et al*. Roles of interlayers in efficient organic photovoltaic devices. *Macromol Rapid Commun.* **2010**, *31*, 2095-2108. DOI : https ://doi.org/10.1002/marc.201000310

[33] Lai, T-H.; Tsang, S-W.; R. Manders, J. *et al*. Properties of interlayer for organic photovoltaics. *Materials Today*. **2013**, *16*, 424-432. DOI: https://doi.org/10.1016/j.mattod.2013.10.001

[34] Duan, C.; Zhong, C.; Huang, F. *et al*. Organic Solar Cells, Materials and Device Physics. Chapter 3: Interface Engineering for High Performance Bulk-Heterojunction Polymeric Solar Cells. *Green Energy and Technology*. Springer-Verlag, London. **2013**. 1-16. DOI: 10.1007/978-1-4471-4823-4_3

[35] Yeh, N.; Yeh, P. Organic solar cells: Their developments and potentials. *Renewable and Sustainable Energy Reviews*. **2013**, *21*, 421-431. DOI: https://doi.org/10.1016/j.rser.2012.12.046

[36] Riordan, C.; Hulstron, R. What is an air mass 1.5 spectrum? (solar cell performance calculations). *IEEE Conference on Photovoltaic Specialists*. **1990**, *2*, 1085-1088. DOI: https://doi.org/10.1109/PVSC.1990.111784

[37] Xu, T.; Qiao, Q. Encyclopedia of Nanotechnology. Chapter O: Organic Photovoltaics: Basic Concepts and Device Physics. *Springer, Dordrecht*. **2012**. 2022-2031.

[38] Kamran, M. Renewable Energy Conversion Systems. Chapter 4: Solar energy. *Elsevier Inc.* **2021**. 109-152.

[39] Qi, B.; Wang, J. Fill factor in organic solar cells. *Physical Chemistry Chemical Physics*. **2013**, *15*, 8972-8982. DOI: https://doi.org/10.1039/C3CP51383A

[40] Feng, L.; Yuan, J.; Zhang, Z. Thieno[3,2-b]pyrrolo Fused Pentacyclic Benzotriazole Based Acceptor for Efficient Organic Photovoltaics. *ACS Applied Materials and Interfaces*. **2017**, *9*, 31985-31992. DOI: https://doi.org/10.1021/acsami.7b10995

[41] Qiu, D.; A. Adil, M.; Lu, K. *et al*. The Crystallinity Control of Polymer Donor Materials for High Performance Organic Solar Cells. *Frontiers in Chemistry*. **2020**, *8*, 603134. DOI: https://doi.org/10.3389/fchem.2020.603134

[42] Cheng, P.; Li, G.; Zhan, X. *et al*. Next-generation organic photovoltaics based on non-fullerene acceptors. *Nature Photonics.* **2018**, *12*, 131-142. DOI: https://doi.org/10.1038/s41566-018-0104-9

[43] Li, D.; Zhang, X.; Liu, D. *et al*. Aggregation of non-fullerene acceptors in organic solar cells. *Journal of Materials Chemistry A*. **2020**, *8*, 15607-15619. DOI: https://doi.org/10.1039/D0TA03703F

[44] Li, S.; Li, C-Z.; Shi, M. *et al.* New Phase for Organic Solar Cell Researches: Emergence of Y-Series Electron Acceptors and Their Perspectives. *ACS Energy Letters.* **2020**, *5*, 1554-1567. DOI: https://doi.org/10.1021/acsenergylett.0c00537

[45] Kan, B.; Kan, Y.; Zuo, L. *et al*. Recent progress on all-small molecule organic solar cells using small-molecule nonfullerene acceptors. *InfoMat.* **2020**, *3*, 175-200. DOI: https ://doi.org/10.1002/inf2.12163

[46] A. Vydrov, O.; E. Scuseria, G. Assessment of a long-range corrected hybrid functional. *The Journal of Chemical Physics.* **2006**, *125*, 234109. DOI: https://doi.org/10.1063/1.2409292

[47] Risko, C.; Brédas, J-L. Multiscale Modelling of Organic and Hybrid Photovoltaics. Chapter 1: Small Optical Gap Molecules and Polymers: Using Theory to Design More Efficient Materials for Organic Photovoltaics. *Springer*. **2013**, 1-38. DOI: https://doi.org/10.1007/128_2013_459

[48] Chigo-Anota, E.; A. Alejandro, M.; B. Hernàndez, A. *et al*. Long range corrected-PBE based analysis of the H_2O adsorption on magnetic BC_3 nanosheets. *RSC Advances*. **2016**, *6*, 20409. DOI: 10.1039/c5ra27231a

[49] Frisch, M.; Trucks, G.; Cheeseman, J. *et al*. Gaussian 16 Rev.A.03 Release Notes. **2017**. URL: https://gaussian.com/relnotes_a03/

[50] Yuan, J.; Zhang, Y.; Zhou, L. *et al.* Single-Junction Organic Solar Cell with over 15% Efficiency Using Fused-Ring Acceptor with Electron-Deficient Core. *Joule*. **2019**, *3*, 1140-1151. DOI: https ://doi.org/10.1016/j.joule.2019.01.004

[51] Cui, Y.; Yao, H.; Zhang, J. *et al*. Over 16% efficiency organic photovoltaic cells enabled by a chlorinated acceptor with increased open-circuit voltages. *Nature Communications.* **2019**, *10*, 2515. DOI: https ://doi.org/10.1038/s41467-019-10351-5

[52] Wei, Q.; Yuan, J.; Yi, Y. *et al*. Y6 and its derivatives: molecular design and physical mechanism. *National Science Review*. **2021**, *8*. DOI: https ://doi.org/10.1093/nsr/nwab121

[53] Mennucci, B. Polarizable continuum model. *Wires Computational Molecular Science*. **2012**, *2*, 386-404. DOI: 10.1002/wcms.1086

[54] Mennucci, B.; Tomasi, J.; Cammi, R. *et al*. Polarizable Continuum Model (PCM) Calculations of Solvent Effects on Optical Rotations of Chiral Molecules. *The Journal of Physical Chemistry A*. **2002**, *106*, 6102-6113. DOI: 10.1021/jp020124t

[55] Lipparini, F.; Scalmani, G.; Mennucci, B. *et al*. Self-Consistent Field and Polarizable Continuum Model: A New Strategy of Solution for the Coupled Equations. *Journal of Chemical Theory and Computation*. **2011**, *7*, 610-617. DOI: https://doi.org/10.1021/ct1005906

[56] Han, G.; Hu, T.; Yi, Y. Reducing the Singlet-Triplet Energy Gap by End-Group Stacking Toward High-Efficiency Organic Photovoltaics. *Advanced Materials.* **2020**, *32*, 2000975. DOI: https://doi.org/10.1002/adma.202000975

[57] Dey, S. Recent Progress in Molecular Design of Fused Ring Electron Acceptors for Organic Solar Cells. *Small*. **2019**, *15*, 1900134. DOI: https://doi.org/10.1002/smll.201900134

[58] Yan, J.; Rodriguez-Martinez, X.; Pearce, D. *et al*. Identifying structure-absorption relationships and predicting absorption strength of non-fullerene acceptors for organic photovoltaics. *Energy & Environmental Science.* **2022**, *15*, 2958. DOI: 10.1039/d2ee00887d

[59] Londi, G.; Dilmurat, R.; D'Avino, G. *et al.* Comprehensive modelling study of singlet exciton diffusion in donor-acceptor dyads: when small changes in chemical structure matter. *Physical Chemistry Chemical Physics*. **2019**, *21*, 25023-25034. DOI: 10.1039/c9cp05201a

[60] Yang, J.; Geng, Y.; Li, J. *et al*. A-DA'D-A-Type Non-fullerene Acceptors Containing a Fused Heptacyclic Ring for Poly(3-hexylthiophene)-Based Polymer Solar Cells. *The Journal of Physical Chemistry C*. **2020**, *124*, 24616–24623. DOI: https://doi.org/10.1021/acs.jpcc.0c07162

[61] H. Park, S.; Y. Kwon, N.; J. Kim, H. *et al*. Nonhalogenated Solvent-Processed High-Performance Indoor Photovoltaics Made of New Conjugated Terpolymers with Optimized Monomer Compositions. *ACS Applied Materials & Interfaces.* **2021**, *13*, 13487-13498. DOI: https://doi.org/10.1021/acsami.0c22946

[62] Picollo, M.; Aceto, M.; Vitorino, T. UV-Vis spectroscopy. *Physical Sciences Reviews*. **2018**, *0*, 1-14. DOI: https://doi.org/10.1515/psr-2018-0008

[63] Itagaki, H. Experimental Methods in Polymer Science - Modern methods in Polymer, Research and Technology. Chapter 3: Fluorescence Spectroscopy. *Elsevier Inc*. **2000**, 155-260. DOI: https://doi.org/10.1016/B978-0-08-050612-8.50009-X

[64] Mahjabin, S.; M. Haque, Md.; Khan, S. *et al*. Effects of oxygen concentration variation on the structural and optical properties of reactive sputtered WOx thin film. *Solar Energy.* **2021**, *222*, 202-211. DOI: https://doi.org/10.1016/j.solener.2021.05.031

[65] Ma, L.; Xu, Y.; Zu, Y. *et al*. A ternary organic solar cell with 300 nm thick active layer shows over 14% efficiency. *Science China Chemistry*. **2020,** *63*, 21-27. DOI: https://doi.org/10.1007/s11426-019-9556-7

[66] Zhang, S.; Qin, Y.; Zhu, J. *et al*. Over 14% Efficiency in Polymer Solar Cells Enabled by a Chlorinated Polymer Donor. *Advanced Materials*. **2018**, *30*, 1800868. DOI: https://doi.org/10.1002/adma.201800868

[67] Hori, T.; Moritou, H.; Fukuoka, N. *et al*. Photovoltaic Properties in Interpenetrating Heterojunction Organic Solar Cells Utilizing MoO_3 and ZnO Charge Transport Buffer Layers. *Materials*. **2010**, *3*, 4915-4921. DOI: 10.3390/ma3114915

[68] Song, J.; Zheng, E.; Wang, X-F. *et al*. Low-temperature-processed ZnO-SnO_2 nanocomposite for efficient planar perovskite solar cells. *Solar Energy Materials & Solar Cells*. **2016**, *144*, 623-630. DOI: https://doi.org/10.1016/j.solmat.2015.09.054